Investigation of Heat-Flux in High Enthalpy Hypersonic Flow Over a Rearward-Facing Step

Deepak N Ramanath*, Sudhir L Gai† and Andrew J Neely‡
School of Engineering & IT, University of New South Wales,
Australian Defence Force Academy Canberra 2600, Australia
[d.ramanath@adfa.edu.au, s.gai@adfa.edu.au & a.neely@adfa.edu.au]

Abstract
Hypersonic laminar flow past a rearward facing step has been numerically investigated using computational fluid dynamics (CFD). The flow parameters were : total specific enthalpy $h_o \approx 26$ MJ/kg; unit Reynolds number Re $\approx 1.82 \times 10^6$ 1/m ; and Mach number $M_\infty \approx 7.6$. A detailed grid independent study has been carried out to investigate the sensitivity of the surface heat flux in the regions of separation and reattachment. The nature of the flow in the close vicinity of the step is particularly emphasised. The influence of real-gas effects such as the thermal and chemical non-equilibrium are studied using Park's two-temperature model and finite-rate chemistry models respectively. The numerical results are then compared with the available experimental data of surface heat flux measurements.

Keywords: CFD, high enthalpy, hypersonic flow, rearward facing step

1. INTRODUCTION

A rearward-facing step is a classical configuration for investigating separated flows. Notwithstanding its simple configuration, it typifies separated flows in many regions of a hypersonic vehicle. Typically for a vehicle under hypersonic regime, the velocities and altitudes at which they operate are severe and the vehicle inherently experience significant heating loads. This is a result of flow separation, dissociation and ionisation, influenced by the molecular excitation/chemical reactions of the gas particles within the flow. These flow and thermo-chemical behaviour predominantly occur at high enthalpy flow conditions. Therefore, understanding the physics of separated flow-field under high enthalpy conditions over a simple configuration such as the rearward-facing step becomes of particular interest. A two-dimensional flow-field is considered here for analysis and a state-of-the-art computational fluid dynamic (CFD) approach is used. The CFD results are then compared with the available experimental data in the region downstream of the step. Although hypersonic flow past a rearward facing step has been experimentally studied in the past in cold wind tunnels, the data at high enthalpy flows where thermo-chemical effects become important is sparse. [1, 2]

The flow past a rearward facing step is characterised by a strong expansion over the corner and separation region downstream of the step and subsequent reattachment with a large shear-layer growth. A general schematic representation of the flow over the step is shown in Fig. 1. The boundary layer upstream of the corner is a consequence of the flow on the surface upstream of the step. As the flow approaches the lip of the step, a strong expansion occurs at the sharp corner and the boundary layer separates. The shear-layer that is formed flows downstream with the formation of a re-circulating region. Few step heights downstream from the step, the shear-layer reattaches with the formation of a

*Postgraduate Student, School of Engineering & IT, UNSW, ADFA
†Visiting Senior Research Fellow, School of Engineering & IT, UNSW, AFDA
‡Senior Lecturer, School of Engineering & IT, UNSW, ADFA

recompression shock wave. A new boundary layer grows from the reattached shear layer. Depending on the flow Mach number and Reynolds number, the flow on the top corner may over expand resulting in a lip shock which eventually coalesces with the recompression shock.

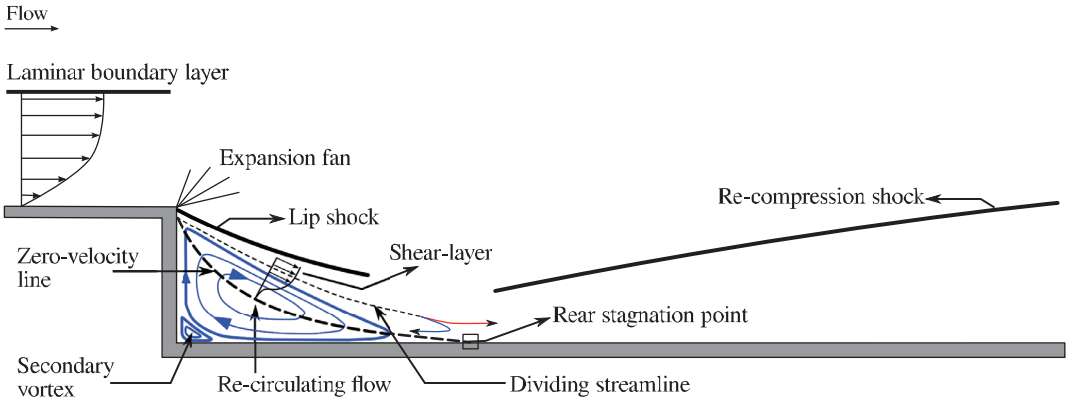

Figure 1. Schematic representation of the flow behind a rearward-facing step

2. GEOMETRY AND FLOW CONDITIONS

2.1. Background

A limited numerical work on a rearward-facing step in a high enthalpy flow was recently carried out by Hillier and is discussed in Hayne et al. [2]. The current investigation extends this work. Firstly, a detailed CFD study is carried out for the same configuration in order to facilitate a direct comparison. Secondly, the study is aimed as a validation benchmark for the type of flow and geometry considered here. Details of the approach along with results are presented in the following sections.

2.2. Geometric configuration & Flow Details

The geometry consists of an upstream flat-plate of length (L) of 48.4 *mm* with sharp leading edge. This is followed by a step of height (h) 2 *mm* and then a flat plate of length (D) of 109.4 *mm*. A schematic representation of the geometry is shown in Fig. 2. The ratio of step height (h) to upstream length (L) is defined by $\tau = h/L$ and has a value of 0.041.

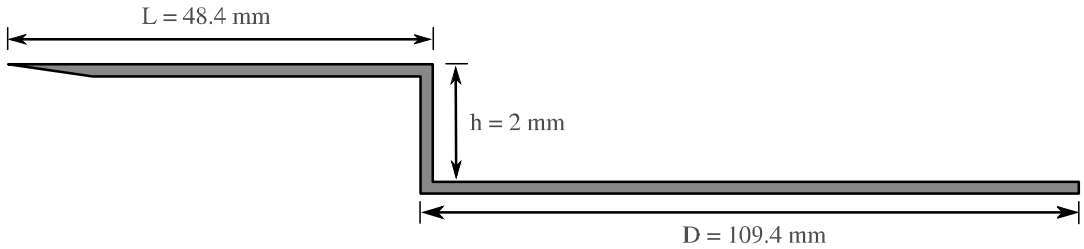

Figure 2. Schematic representation of 2 mm rearward-facing step

The experimental work associated with this configuration was conducted in the University of Queensland, X2 expansion tube facility with air as the test gas [2]. The available test times in X2 is of the order ≈ 90 μs [3]. Due to this short duration limitation, the primary concern is whether steady flow over the flat plate and subsequent steady separated flow behind the step can be achieved. Establishment time varies with respect to the scale of the separated region and larger the step or the base height, the

establishment time is known to increase [4]. Hence, a step height of 2 *mm* was primarily chosen for the experiments in order to ensure steady separated flow [3]. In some of the previous experimental studies [1, 5, 6] over rearward facing steps in short duration facilities, small step heights were chosen to facilitate these criteria. In the current investigation, since a direct comparison of the experimental data by Hayne [3] and numerical data by Hillier [2] are made, identical geometric configuration has been subjected to computational study.

The preliminary results by Hayne et al. [2] for this configuration were at a total specific enthalpy of 30 *MJ*/*kg* and unit Reynolds number of $3.35 \times 10^6 m^{-1}$ and is referred here in as *condition A*. These conditions were used by Hillier in Ref. [2] to carry out the preliminary numerical simulations. To be consistent then, flow properties of condition A were used for CFD calculations in the present investigation to carry out a grid independence study so as to compare the numerical results of Hillier [2]. Some of the freestream parameters for condition A have also been evaluated from Gai et al. [6]. Subsequent CFD analysis is based on the freestream conditions used by Hayne [3] to obtain his experimental data in the same X2 expansion tube facility. These later flow conditions are designated here as *condition B*, with a total specific enthalpy of 26 *MJ*/*kg* and a unit Reynolds number of

$1.82 \times 10^6 m^{-1}$. Details of both the conditions are given in Table 1. For the flow condition B, Hayne[3] has conducted a detailed evaluation of the test gas properties assuming both equilibrium and non-equilibrium behaviour. The test gas composition as a result of non-equilibrium analysis is given in Table 2.The test duration available for both the flow conditions were approximately between 85-90 μs [3]. As can be seen from the examination of the two flow conditions in Table 1, the differences in the flow properties are minor except the values of freestream temperature and the frozen γ_f. However, these differences should not seriously influence the gross properties such as pressure and heat flux.

Table 1. Freestream conditions

Condition	h_o	Re_L	M_∞	p_∞	T_∞	U_∞	ρ_∞	γ_f	T_w/T_o
	MJ/kg	$1/m$		Pa	K	m/s	kg/m^3		
A	≈ 30	3.35×10^6	9.1	8.30×10^3	1041	6700	21.90×10^{-3}	1.42	0.019
B	≈ 26	1.82×10^6	7.6	10.4×10^3	1813	6872	17.32×10^{-3}	1.34	0.015

Table 2. Test gas composition for condition B

Species	Mass fraction ($x_{i\infty}$)
N_2	0.770
O_2	0.050
N	0.000
O	0.160
NO	0.020

3. COMPUTATIONAL APPROACH

The two-dimensional flow-field of interest was modelled using two compressible Navier-Stokes solvers, MB-CNS-2[7] and Eilmer-3[8] which are based on Multi-Block approach. MB-CNS is a time-dependent, compressible, viscous, two-dimensional solver capable of solving laminar, turbulent and chemically reactive flows. Eilmer-3 on the other hand, is a three-dimensional solver having similar capabilities as that of MB-CNS in addition to modelling thermal non-equilibrium behaviour of the flow. This is based on the well known two-temperature model of Park [9], where the coupling between translation-rotational and vibrational-relaxation temperatures is taken into account ($T_r - T_v$). MB-CNS

and Eilmer compute at cell-centres and use explicit time stepping to update the conserved quantities. A modified van Albada limiter and MUSCL (Monotone Upstream-centered Schemes for Conservation Laws) reconstruction scheme [10] are used to obtain second-order spatial accuracy. To calculate the mass, momentum and energy flux between finite volume cells, the advection upwind splitting method combining difference and vector splitting (AUSMDV), is used [11]. A full description of the basic equations and algorithms used for the single-block is reported in Jacobs [12] and multi-block is reported in Jacobs [7]. MB-CNS is extensively validated for high enthalpy hypersonic flows at suborbital and superorbital conditions including equilibrium and finite rate chemistry. Details of the code verification and validation are reported in references [13, 14, 15, 16, 17]. Both MBCNS and Eilmer have capabilities to solve the multi-block grids utilising multiple CPU through Message Passing Interface (MPI)[18]. Therefore, the CFD calculations were accordingly performed on multiple CPUs.

For the grid independence study, laminar CFD calculations were performed under the assumption of perfect-gas for condition A. The test gas air was considered as a single species while the thermodynamic behaviour was calorically perfect with a constant ratio of specific heats (γ). Transport properties were evaluated using the Sutherland formulation. For condition B, in addition to perfect-gas calculation, chemical and thermal non-equilibrium effects were taken into consideration where the test gas air was modelled as 5 species. The mass fractions of these are given in Table 2. In the context of modelling chemical and thermal effects, two schemes were used. In the first, the finite-rate chemistry was modelled based on the kinetic scheme of Gupta et al. [19], while in the second, both finite-rate chemistry and two-temperature thermal behaviour was based on Park's [9] kinetic mechanism. In both cases, only the neutral reactions were modelled neglecting the effects of ionisation. Details of finite-rate chemical reactions are give in Table 3 and the vibrational-relaxation rates for thermal coupling can be found in Park [9].

The reason for using these two models is that they have been used previously by a number of researchers [20, 21, 22, 23, 24] and have been found to give reasonably reliable results.

Table 3. Finite-rate chemistry reaction schemes for condition B

Gupta et al. [19]	Park [9]
$O_2 + M \rightleftharpoons O + O + M$	$N_2 + M \rightleftharpoons N + N + M$
$N_2 + M \rightleftharpoons N + N + M$	$O_2 + M \rightleftharpoons O + O + M$
$N_2 + N \rightleftharpoons N + N + N$	$NO + M \rightleftharpoons N + O + M$
$NO + M \rightleftharpoons N + O + M$	$NO + O \rightleftharpoons O_2 + N$
$NO + O \rightleftharpoons O_2 + N$	$N_2 + O \rightleftharpoons NO + N$
$N_2 + O \rightleftharpoons NO + N$	-

The thermodynamic behaviour and transport properties for the chemical and thermal non-equilibrium calculations were modelled as follows. Thermo-chemically, the gas is treated as a mixture of thermally perfect gasses, where c_p and c_v are functions of temperature. The values of c_p and c_v are obtained from polynomial curve fits suggested by Gordon et al. [25] which are valid up to 20,000 K. The least squares curve fits of Gordon et al. [25] are used to compute viscosity and thermal conductivity of individual species that are valid up to 20,000 K and is based on collision-integrals model. Transport properties of the species mixture are then calculated using the method adopted by Gordon et al. [25] that utilises interaction potential between each of the species. Modelling of chemical non-equilibrium reactive flows were achieved by using the timestep-splitting method as reported in Rowan [26]. The integration scheme, a quasi-steady state method [27] was used to solve a set of *stiff* ordinary differential equations. Diffusion velocities were modelled using Fick's Law.

The basic coordinate system for the step configuration is shown in Fig. 3 in reference to the geometry. Here, the forebody, step and the downstream plate surfaces are expressed in terms of a

continuous wetted surface, [*s*] as shown in Fig. 3(a). They are then normalised by the step height (*h*), and referenced such that *s*/*h* = 0 represents the step top corner and *s*/*h* = 1 the bottom corner respectively. Details are shown in Fig. 3(b). Consequently, based on the geometric dimensions, the leading edge of the forebody attains a value *s*/*h* = –24.20 and *s*/*h* = 55.7 for the trailing edge of the downstream plate.

A CGNS (cfd general notation system) multi-block structured grid was developed for this problem using a commercial code ICEM-CFD [28]. Fig. 4 shows the computational domain and the topology. The multi-block grid consisted of 8 blocks which are interconnected node-to-node precisely. As shown in Fig. 4, the far upstream block has a free-slip wall (not indicated in Fig. 4). This ensures that the boundary layer growth from the sharp-leading edge is not affected. The leading edge shock angle is initially determined through solving a coarser domain of a rearward facing-step that has a rectangular block (figure not shown). The external boundary for the inflow is then approximately aligned to the leading edge shock angle and it is ensured that the inflow boundary does not interfere with the leading edge shock. Structured grids aligned in this fashion capture the gradients of shock very well and are known to improve convergence. The upstream flat plate, step and the downstream flat plate are modelled as a cold wall with a fixed temperature of T_w = 300*K*. The top external boundaries are used to provide uniform supersonic inlets and the supersonic outlet is provided at the trailing edge of the downstream plate. As can be seen from Fig. 4, the present computational domain extends up to 54 step heights from the step which covers the entire downstream region of the experimental model. This is much greater than the 20 step heights considered by Hillier in Hayne et al.[2].

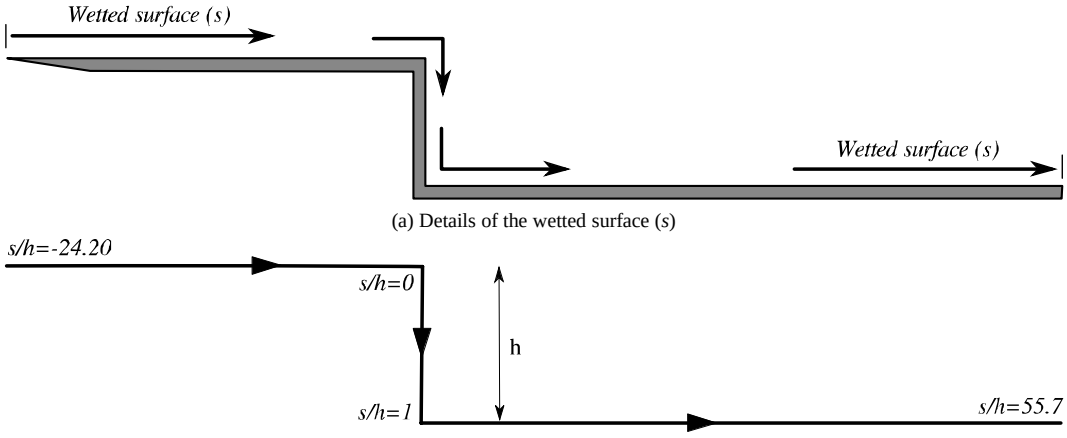

Figure 3. Schematic of the coordinate system for the step

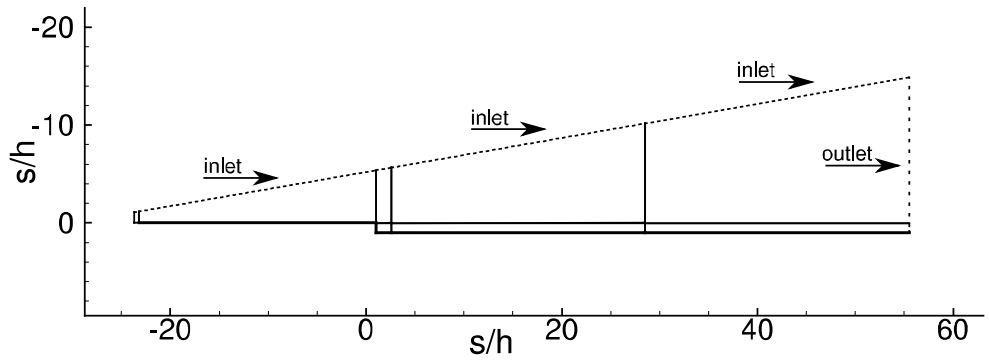

Figure 4. Grid topology and Boundary conditions for a 2 *mm* step

A grid independence study is carried out for the computations with condition A and follows the approach used by Jackson et al. [29]. Their work particularly focuses on hypersonic perfect gas cavity flows but is of relevance here for two reasons. Firstly, the flow solver used is the same as that used for the computations in Hayne et al. [2]. Secondly, Jackson et al. [29] present a comprehensive grid independence study for a 25 *mm* cavity that is meant to validate against experimental data. Jackson et al. [29] consider surface heat flux as one of the variable in determining grid independence as it is said to provide a sensitive test for CFD calculations. In the present investigation also, surface heat flux is chosen in determining grid independence. The initial grid (G1) comprises of 60 *i*–× 25 *j*– cells with a first cell height from the wall, $\Delta_w = 100\mu m$. Initialisation of the flow was performed with zero velocity and a pressure of 50 Pa, similar to the conditions that exists in the test section at $t = 0$ seconds. The flow was simulated for a total experimental run time of 90 μs with a time marching at every 5×10^{-10} seconds. Surface heat flux was computed on the upstream flat-plate (*L*), step-face (*h*) and the downstream wall (*D*). Subsequent refinement of the grid was then performed where the cells in both *i*– and *j*– directions were doubled and Δ_w was reduced by a factor of 0.5. Details of the grids along with Δ_w relevant to each grid is presented in Table 4. The region bounded within the step-face and approximate reattachment location is referred here as the *vicinity of the step* (VOS) and is also referred to the cells within this region. A bi-geometric expansion law [28] is used for the cells that extend from the wall with an expansion factor of 1.1. This ensures that sufficient cells are placed close to the wall in order to capture a solution with good resolution. This is particularly important for the location of separation, reattachment and the recirculating region. This is illustrated in Fig. 5 for G-5. Jackson et al. [29] point out that this type of refinement is quite critical for shear layer and heat flux predictions at these locations.

Table 4. Various grids used for the grid independent study

Grid	$i- \times j-$	$\triangle_w$	VOS
G-1	60×25	$100\ \mu m$	10×10
G-2	120×50	$50\ \mu m$	20×20
G-3	240×100	$25\ \mu m$	27×40
G-4	288×120	$20\ \mu m$	46×48
G-5	410×120	$20\ \mu m$	80×48
G-6	410×152	$20\ \mu m$	80×90

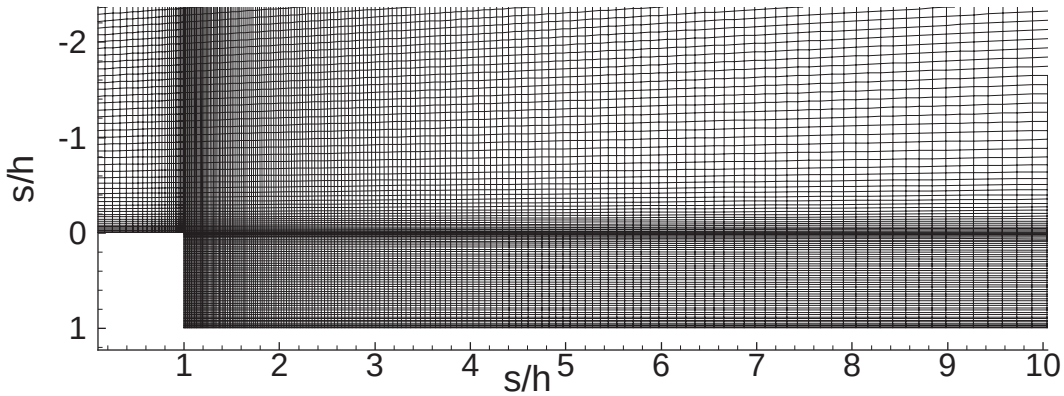

Figure 5. Details of the grid in the vicinity of the step

The heat flux predictions on the flat plate as the flow approaches the top corner and on the step face is shown in Fig. 6 for grids G1 to G-6. Here $s/h = 0$ and $s/h = 1$ represent the top and bottom corner of the step respectively. Surface heat flux (q_w) is estimated from equation 1 with the units w/cm^2. The thermal conductivity (k) was based on the average value between the wall and the first cell from wall. Similarly, the heat flux behind the step from $1 \leq s/h \leq 55$ is computed using equation 1 which is presented in Fig. 7 for the grids G-1 to G-6.

$$q_w = k\left[\frac{\partial T}{\partial y}\right]_{y=0} \tag{1}$$

The CFD heat flux results presented in Fig. 6 provide a good indication of grid sensitivity for the upstream portion of the flat-plate and the step face. The region between $-0.5 \leq s/h \leq 0$ is quite close to the top corner and any variation in heat flux distribution is shown magnified compared to considering the entire length of the plate. Furthermore, the prediction of the gas properties close to the top corner is critical as this could directly influence the flow physics downstream of the corner. As can be noted from Fig. 6, there is very little variation in heat flux between grids G-3 to G-6 from $-0.5 \leq s/h \leq 0$. Surface heat flux distribution on the step-face between $0 \leq s/h \leq 1$ also show very little variation for grids G-3 to G-6. However, it should be noted that these heat flux data are not validated against experimental results as no experimental data is available in such close proximity of the top corner and on the step-face. The increase in heat flux as the top corner is approached is due to the favourable pressure gradient that the boundary layer experiences in the vicinity of the corner. Behind the step for $s/h \geq 1$, the heat flux results are compared with the CFD data in Hayne et al. [2] and are discussed below. Experimental validation of the region, $s/h \geq 1$ is presented and discussed in the later sections.

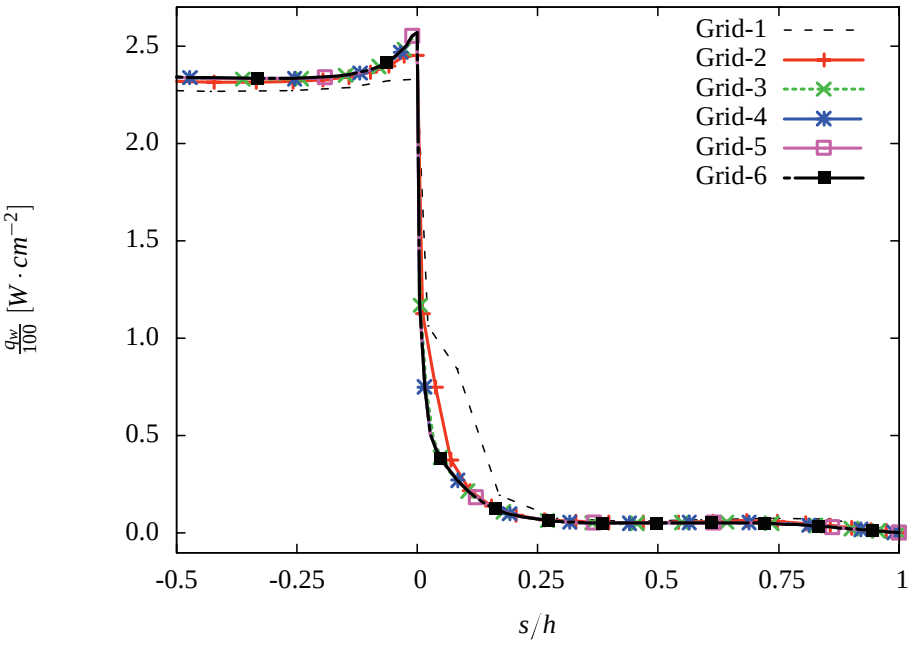

Figure 6. Surface heat flux distribution upstream and on the face of the step, $-0.5 \leq s/h \leq 1$

Referring to Fig. 7, the grid corresponding to G-3 has similar number of cells to that in Hayne et al. [2] in the vicinity of the step, i.e. 40 i– × 40 j–. The following remarks are in order. While the two predictions, the present G-3 to G-6 and those in Hayne et al.[2] are close within about 4 step heights,

they differ considerably further downstream. Possible explanation for this could be due to the value of Δ_w in G-3 to G-6 which is $\leq 25\mu m$. The temperature gradient from the wall to the first cell from wall is critical in estimating the heat flux. This could be clearly seen from Fig. 7 comparing G-4, G-5 and G-6. Here, Δ_w has a value of $20\mu m$ and thus predicts same heat flux distribution. Now between G-4 and G-5, the grids in the step has a variation only in the *i*– (streamwise) direction and the cells in the VOS are nearly doubled in *i*– direction (refer Table 4). Heat flux distribution is however the same for both these grids. In contrast, G-5 and G-6 has a variation in *j*– (flow normal) direction, where cells in the VOS are also nearly doubled. But, the heat flux distributions are the same as that of G-4 and G-5. Therefore, heat flux distribution is found to be insensitive in the streamwise direction between G-4 and G-5. Similarly the heat flux distribution between G-4 and G-5 is found to be insensitive in the normal direction. This supports the idea that the surface heat flux is indeed sensitive to only Δ_w, i.e. first cell height from wall when sufficient cells are clustered near the wall. However, this is in variance with Jackson et al. [29] observation, where in they found heat flux distribution was sensitive also to streamwise cell distribution within the cavity. This could possibly be due to multiple recirculating vortices in a cavity flow that depend on the grids in the streamwise direction. Due to the severe computational time requirement for solving values of Δ_w below $20\mu m$, they were not investigated further.

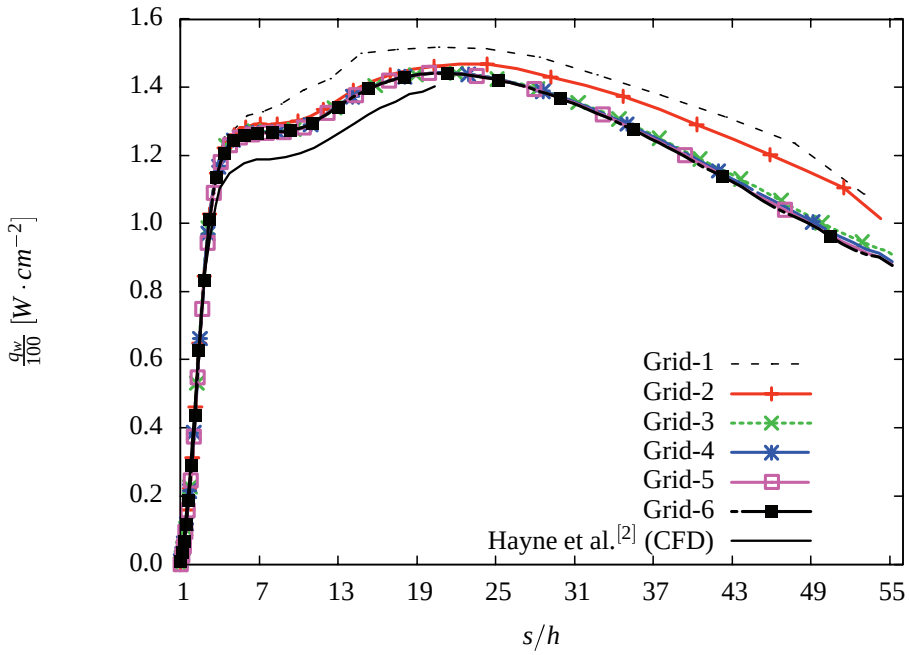

Figure 7. Surface heat flux distribution on the plate downstream of the step, 1.0 ≤s/h ≤55

Skin-friction co-efficient for the forebody in the close vicinity of the top corner (–0.5 ≤s/h ≤0) and the step face (0 ≤ s/h ≤ 1) for different grids are shown in Fig. 8. Skin-friction coefficient is indicative of the wall shear stress that exists due to the viscous boundary layer. Therefore, in addition to heat flux, skin friction was also used to examine the grid sensitivity in the vicinity of the step. From Fig. 8, skin-friction show very little variation between grids G-3 to G-6. Skin-friction co-efficient were next computed for the different grids to check the sensitivity of boundary-layer separation and reattachment locations. This is because, the skin-friction changes from positive value to negative value at separation and vice-versa at reattachment. Hence it should give a good indication of the position of separation at the step and reattachment behind the step. Skin-friction coefficient was calculated using the equation 2.

$$c_f = \frac{2\tau_w}{\rho_\infty {u_\infty}^2} \tag{2}$$

where ρ_∞ and u_∞ are freestream density and velocity respectively. τ_w is the shear stress at the wall, $y = 0$, given by equation 3.

$$\tau_w = \mu_w \left[\frac{\partial u}{\partial y}\right]_{y=0} \tag{3}$$

The viscosity (μ_w) in equation 3 has an average value between wall and the first cell from wall.

Table 5 gives the dimensionless separation and reattachment distance from $s/h = 0$ (top corner) for various grids. Grid convergence index (GCI) based on the generalised theory of Richardson Extrapolation [30] was used to determine the relative error between the grids used. CGI based on Richardson Extrapolation is generally considered to be the standard method for reporting grid uncertainty in numerical simulations involving CFD [31, 32]. In this technique [30], the variable of interest for finer and coarser grid are used to estimate the relative error between them. In Table 5, GCI_s and GCI_r are the relative errors obtained for separation and reattachment locations respectively. It should be noted that the GCI_s between G-6 and G-5 is 4.96E-4 which is extremely small and is zero for GCI_r. For the grids G-6 and G-5, the reattachment location is predicted at $s/h = 2.59$, which is 1.59 step heights from the step face. This is in close agreement to the predictions made in Hayne et al. [2] where in the reattachment distance is given as 1.53. Experimentally it is estimated to be around 1.6 step heights based on holographic interferometric flow visualisation [33]. Both from the surface heat flux and skin-friction coefficient distributions, it would appear that the solution should be grid independent at G-5 and all further computations are calculated using this grid.

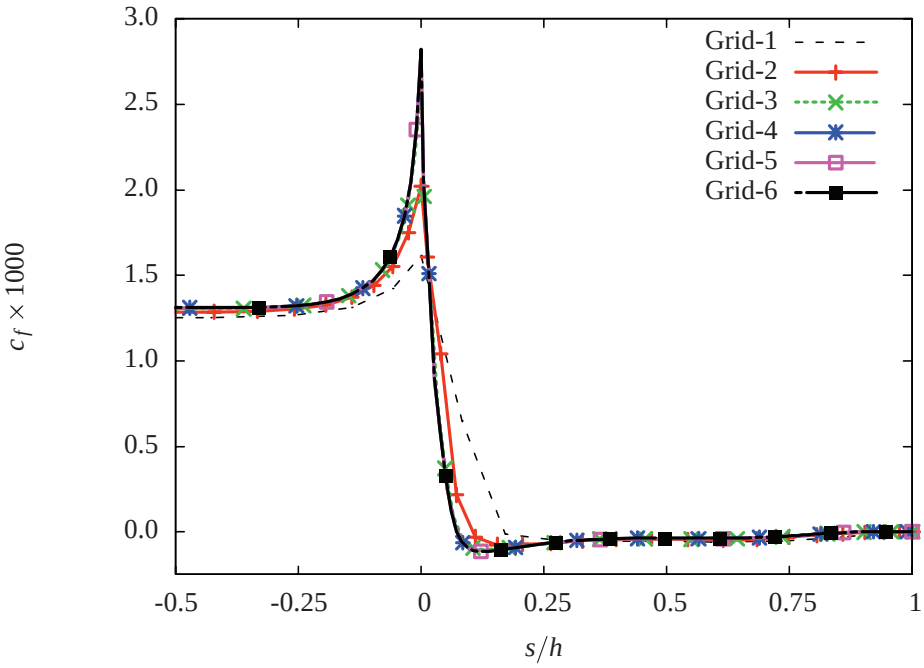

Figure 8. Skin-friction distribution between upstream and on the face of the step, $-0.5 \leq s/h \leq 1$

Table 5. Separation and reattachment distance for various grids

Grid	Separation (s/h)	GCI_s	Reattachment (s/h)	GCI_r
G-1	0.126	4.80E-2	2.48	5.86E-2
G-2	0.090	1.50E-2	2.63	1.83E-2
G-3	0.074	6.66E-3	2.63	4.34E-2
G-4	0.075	2.84E-3	2.60	8.53E-2
G-5	0.075	0.00	2.59	6.55E-3
G-6	0.076	4.96E-4	2.59	0.00

Another important observation from Fig. 8 is that at the lip of the step, the skin friction rises steeply to very large values due to the steeply falling pressure as the corner is approached. As a result of change in boundary conditions at the corner, a singularity is encountered in the solution of the boundary layer equations. This is the well known trailing edge problem and has been treated extensively in the past in incompressible [34, 35, 36] and compressible [37] flows.

4. RESULTS AND DISCUSSIONS

4.1. Flow Separation and Reattachment

The numerical results of time-dependent, two-dimensional flow over a 2*mm* rearward facing step are presented here. The CFD computations initially performed for the purpose of grid independence study were solved for 90μs in order to directly compare with Hillier's data [2]. However, after obtaining the grid independent solution, computation using grid G-5 was repeated for a much longer time of 160μs. During these process, results were extracted every 5μs for up to t = 50μs and from t = 50 –160μs results were obtained at a rate of every 10μs. About 50 -100 step heights flow establishment lengths are generally required [4] to attain steady laminar separated flow behind a step. Based on the freestream conditions, the flow should establish at $t \approx 30\mu s$. In Fig. 9 normalised separation and reattachment distances are presented as the flow develops. Here, (s/h) is normalised with it's steady state value $(s/h)_s$ for separation and $(s/h)_r$ for reattachment. It can be observed from these results, that reattachment takes about 40μs longer to stabilise than the separation. Also, it is interesting to note that the separation location moves down along the face of the step with time before it reaches a steady state. In the case of reattachment, the near wake structure shrinks as the flow establishes resulting in shorter reattachment distance from the step. Considering the formation of boundary layer separation and reattachment, the flow should take a minimum of 70μs (t_{est} ≈240 flow step heights) for achieving a steady state. Therefore, for a total simulation time of 160μs (*test* ≈ 530 flow step heights), a well established steady state condition should exist and all the subsequent results correspond to t = 160μs.

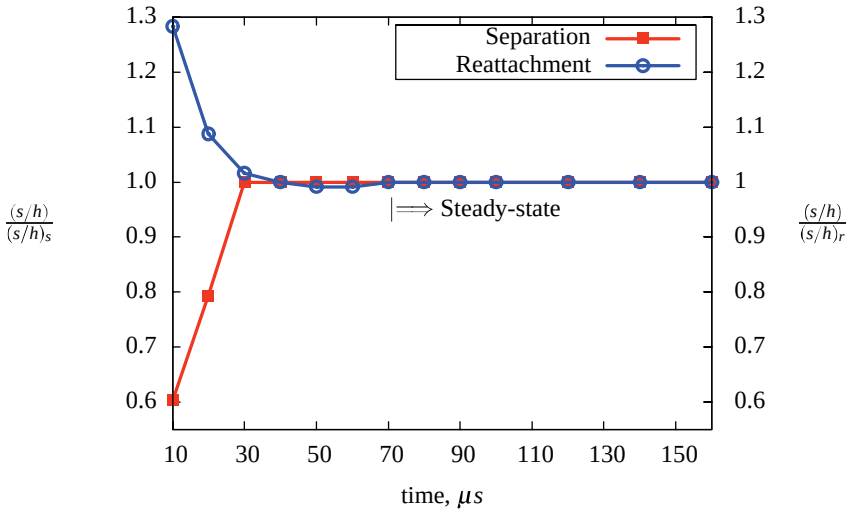

Figure 9. Normalised separation and reattachment flow establishment time

4.2. General flow features

As the flow develops, a weak leading edge shock is formed with a growing boundary layer over the flat plate. This could be visualised from Fig. 10, where Mach contours indicate the general flow features over the entire rearward facing step configuration. The leading edge shock and the boundary layer on the plate are clearly seen. An expansion occurs at the step corner followed by boundary layer separation. As can be seen, a thick separated shear-layer has formed as the flow turns round the corner and expands the flow that scavenges from the separated shear-layer forming a recirculating region at the base of the step. A recompression shock as a result of reattachment is also seen. A close-up of the view of the flow in the immediate vicinity behind the step region is shown in Fig. 11. Due to over expansion of the flow around the top corner, existence of a lip shock embedded within the shear layer is inferred. Hama [38] has studied the formation of the lip shock and has shown that its existence depends on both Mach number and Reynolds number. Although the lip shock is not clearly visible in Figs. 10 or 11 immediately downstream of the step, it seems to emerge well downstream coalesced with the recompression shock as can be visualised about 5 step heights behind. Other features to note are the separation just below the top corner [39] and reattachment on the plate. A thick shear layer [1] trails downstream and a boundary layer subsequent to reattachment seems to have developed. Downstream of reattachment, the shear-layer shows little curvature and is parallel for long distance downstream and this is also evident in experimental results of Gai et al. [1]. Due to difficulty in visualising the lip shock in Figs. 10 and 11 magnitude of density gradient are shown in Fig. 12 in Gray-scale. Density gradient magnitude was obtained by computing $|\nabla\rho| = \sqrt{\rho_x^2 + \rho_y^2}$ over the two dimensional flow field, where, ρ_x and ρ_y are the local density scalars in x and y directions respectively. The convergence of a weak lip shock is now visible as also its coalescence with the reattachment shock within about 3 step heights.

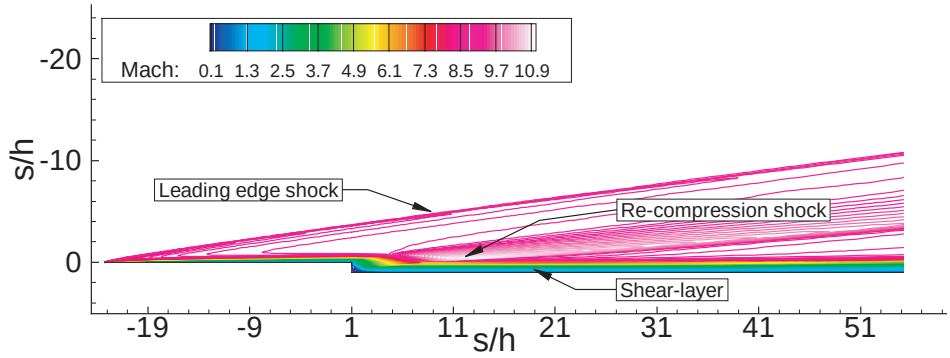

Figure 10. Mach number contours for a 2 *mm* step

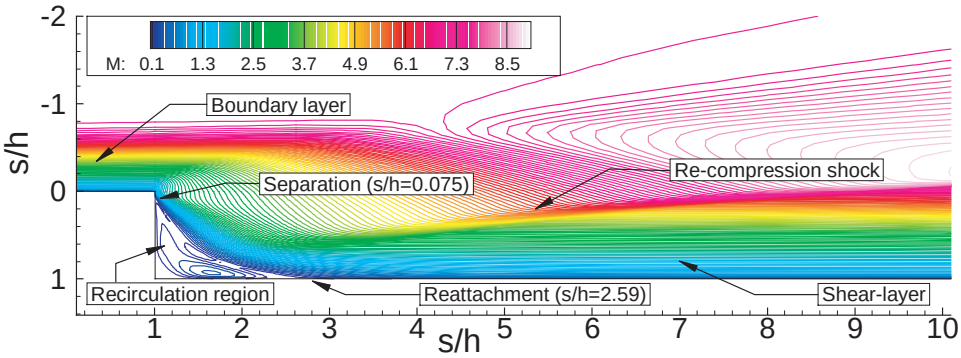

Figure 11. Close-up of Mach number contours behind the step

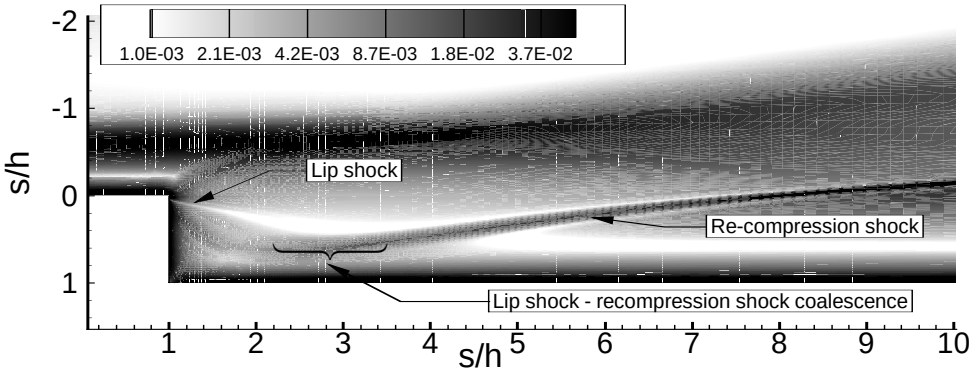

Figure 12. Density gradient magnitude contour behind the step

The streamline pattern illustrated in Fig. 13 shows a subsonic primary vortex and a secondary vortex at the bottom corner. The direction of the primary vortex is clock wise, whereas the corner vortex has a counter-clock wise direction. The presence of the corner vortex is very similar to the secondary eddy observed in cavity driven flows [29]. Separated shear-layer and the scavenged fluid together form a dividing streamline that originates from the separation point. This is clearly seen from the Fig. 13.

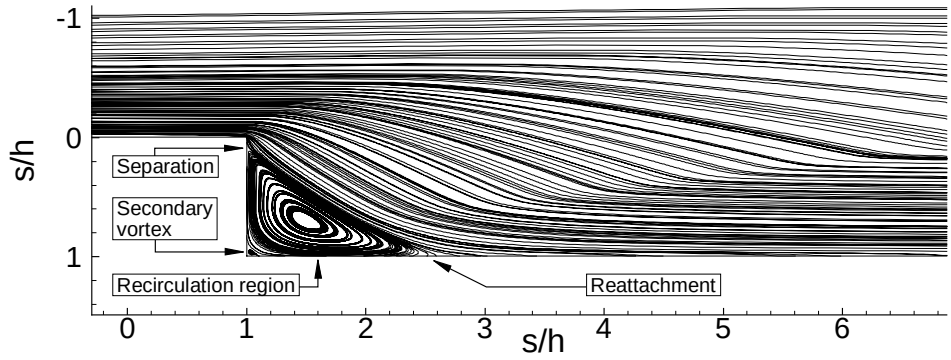

Figure 13. Computed streamlines behind the step

A computational interferogram for the flow behind the step was generated using the computed density. One of the potential advantage with this is that it allows for direct comparison with experimentally obtained interferograms. For the present results, computational interferogram was obtained through the extension of Gladstone-Dale equation [14] that is used to obtain the fringe shift. This is given by equation 4. Here, λ is the wavelength of the laser beam that is used in obtaining experimental interferogram, K_i is the Gladstone-Dale constant for species i and C_i is the species concentration. For the computed interferogram, the value of $K_i = 1.609 \times 10^{-2}$ and $\lambda = 589nm$ were used.

$$F = \int_{z_1}^{z_2} \left[\frac{\rho - \rho_\infty}{\lambda} \sum_{i=1}^{n} K_i C_i \right] dz \tag{4}$$

$$I = cos^2(\pi F + x\delta) \tag{5}$$

The intensity of light across the image was calculated using equation 5 [14], where δ is the offset compensation for any background phase shift between test and reference beams in the experimental interferogram. However, x is the computational spacing in the streamwise direction and is required only

for the computational intensity calculation. Computational interferogram in comparison with experimentally obtained one [2] are shown in Fig. 14. Some of the prominent features to note from both the computed and experimental results are the leading edge shock, the upstream boundary layer, the expansion behind the step and the reattachment shock wave. It may also be noticed that the boundary layer is as thick as the step height.

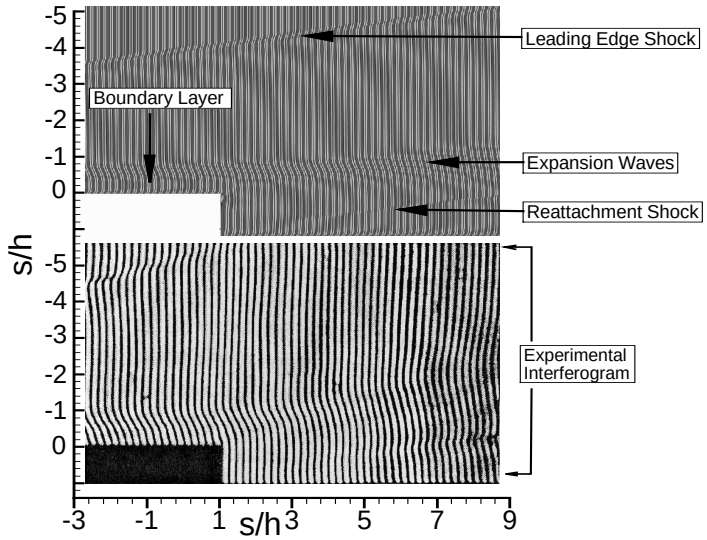

Figure 14: Computational and experimental interferograms for the flow behind a 2 *mm* step

4.3. Heat flux distribution downstream of the step

Fig. 15 shows the CFD results of heat flux in terms of normalised Stanton number (S_t /S_{t-fp}) for the present calculations in comparison with the experimental data [3] downstream from the step, i.e. $s/h \geq 1$. The Stanton number distribution downstream of the step (S_t) are normalised with corresponding attached flat-plate Stanton number (S_{t-fp}) data for both the experimental as well as for the CFD results. The S_{t-fp} distribution for the attached flat-plate in CFD was obtained by solving the computation grid similar to that shown in Fig. 4, where beyond the step region, wall boundary condition was used. This allowed an exact cell-to-cell match between the step and the attached flat-plate computational domains both upstream as well as downstream of the corner. Stanton number distribution shown in Fig. 15 for the step and for the attached flat-plate was evaluated based on the relation given by Hayne [40] and is given in equation 6,

$$S_t = \frac{q_w}{\rho_e u_e (h_r - h_w)} \tag{6}$$

where, q_w was calculated based on equation 1 and thermal conductivity k in equation 1 was evaluated as an average value between wall and the first cell from the wall. The recovery enthalpy (h_r) was subsequently evaluated using equation 7 and h_w represents wall enthalpy. In equation 7, h_e is the enthalpy at the outer edge of the boundary layer and Pr is the Prandtl number evaluated at the wall.

$$h_r = h_e + \sqrt{P_r}\frac{u_e^2}{2} \tag{7}$$

Experimentally, five shots were considered and the details of shot to shot variations are found in Hayne [3]. Using the data of five shots an experimental best-fit curve was constructed. The normalised Stanton number (S_t /S_{t-fp}) distributions of the experimental shots along with the best fit is also shown in Fig. 15.

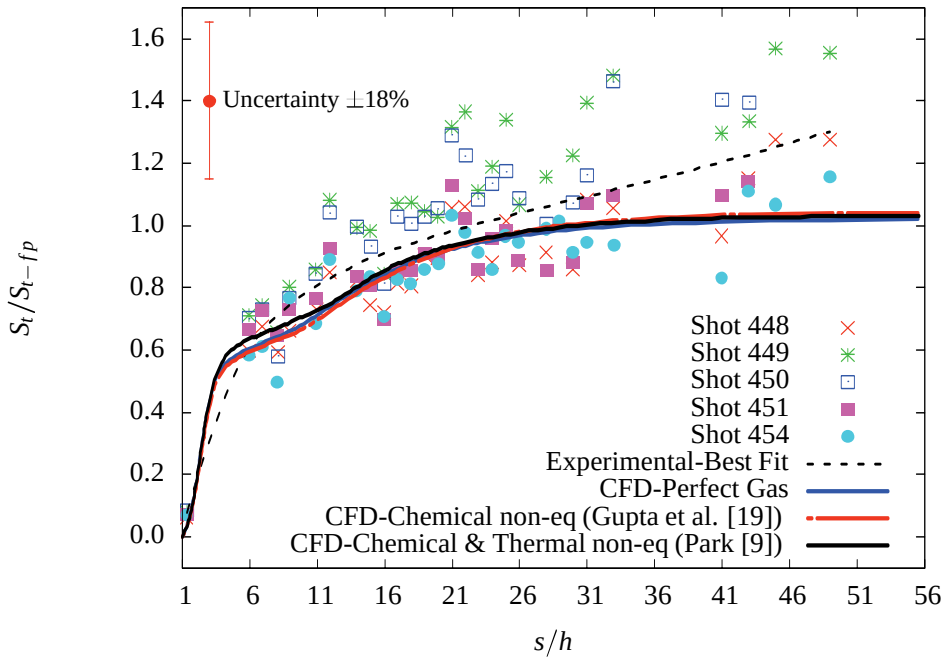

(a) Experimental comparison with CFD results downstream of the step

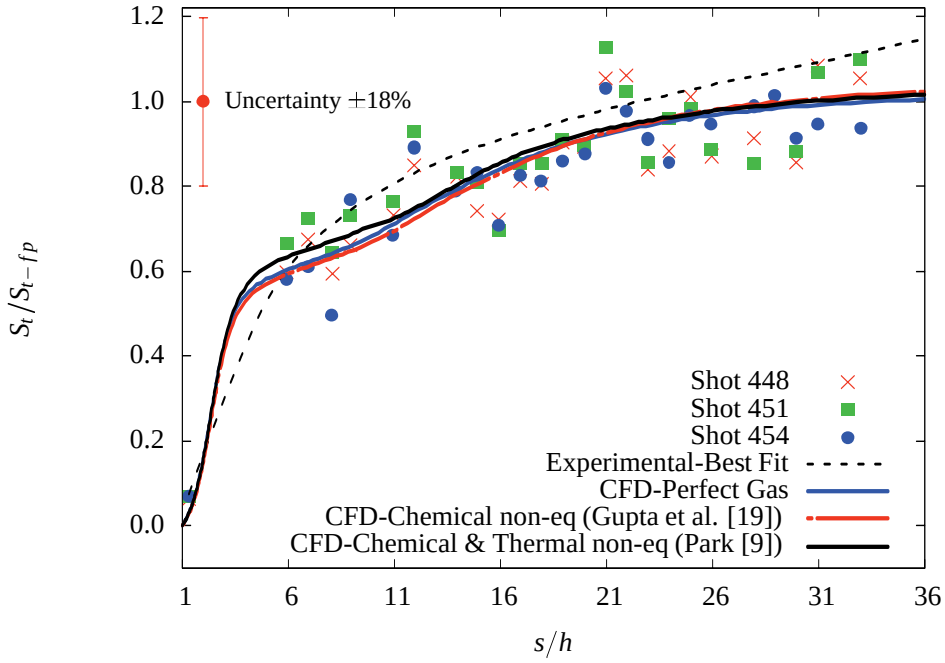

(b) Experimental comparison with CFD between $1 \lesssim s/h \lesssim 36$

Figure 15. Stanton number distribution behind the step

In Fig. 15(a) three sets of CFD data are presented corresponding to perfect-gas, chemical non-equilibrium and chemical plus thermal non-equilibrium calculations respectively. It can be noticed that the CFD data show good agreement with the experiments downstream of the step, especially $s/h \leq 30$. The data of chemical non-equilibrium and chemical plus thermal non-equilibrium do not deviate much

in comparison to perfect-gas and possible reasons for this are discussed in the following paragraphs. Other features to note from Fig. 15(a) are that the CFD data deviate considerably from experiments further downstream after $s/h \geq 30$, while considerably under predicting the S_t / S_{t-fp} values from shots, 449 and 450 respectively. In order to examine the comparison within the region $1 \leq s/h \leq 30$ more clearly, CFD data along with the experiments from shots 448, 451 and 454 are illustrated in Fig. 15(b). It is quite evident that the CFD data generally show good agreement considering the experimental scatter. The experimental data points between the region $2 \leq s/h \leq 6$ are sparse and therefore no direct comparison can be made here. However, CFD predicts the experimental data point at $s/h = 1.3$ immediately past the step very well. The CFD and experimental data show heat-flux approaching zero at the lower corner of the step. This is a characteristic of a two-dimensional laminar flow at a concave corner [29]. Furthermore, the CFD data of perfect-gas and chemical non-equilibrium indicate a distinct plateau region between $3 \leq s/h \leq 11$, although this is not so clear in the case of chemical plus thermal non-equilibrium data. The reason for this could be the result of the emergence of slip-stream when the lip shock coalesces with the recompression shock. Experiments however do not quite give such an indication. CFD results obtained through the modelling of chemical non-equilibrium indicate a lower heat flux when compared to perfect-gas which is to be expected. On the other hand, chemical plus thermal non-equilibrium data predict slightly higher heat flux compared with the perfect gas case but closer to the experimental best fit curve. The reason for this is not clear and is still being investigated.

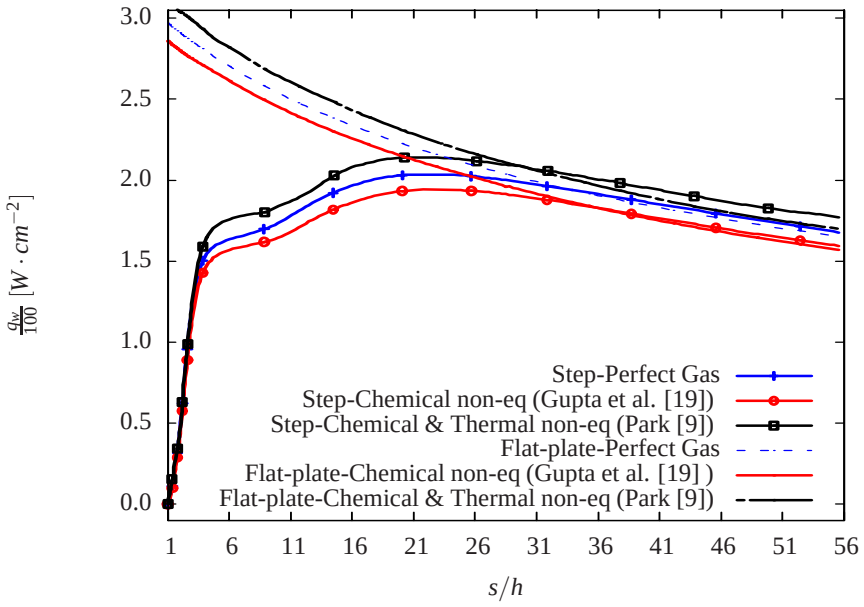

Figure 16. Heat flux data downstream of the step and attached flat plate

To better highlight the influence of individual computational model on heat flux, raw heat flux (q_w) data downstream of the step and its equivalent flat-plate values are presented in Fig. 16. There are several features that can be noted. While all the three models agree with each other from separation to reattachment quite well, differences are evident after $s/h \geq 6$. Firstly, after $s/h \geq 6$, the perfect gas model predicts higher heat flux in comparison with the chemical non-equilibrium (Gupta [19]) model. In contrast, thermal plus chemical non-equilibrium (Park [9]) model predicts higher heat flux than the perfect gas. Secondly, we also note that there is a proportional increase in the flat-plate heat flux data among the three models. Therefore, when the step data is normalised as in Figs. 15(a) and 15(b), not much difference is evident among them. However, the increase noted beyond $s/h \geq 6$ for the thermal plus chemical non-equilibrium model appears to be a consequence of faster rate of reduction in the flat-plate

heat flux when compared to the other two models. This is particularly noticeable beyond $s/h \geq 25$, where the flat-plate q_w predicted through chemical plus thermal non-equilibrium model nearly approaches perfect gas values. This heat flux variation noted between chemical non-equilibrium and chemical plus thermal non-equilibrium models are likely attributed to the manner in which reactions are modelled (see table 3) and also the respective reaction rates.

A plot of species mass fraction (x_i) downstream of the step over the plate wall shown in Fig. 17 illustrates the possibility of variation in chemical kinetics. It is seen that, N_2 concentration remains almost unchanged in both the models. Although, O_2 concentration can be seen to decrease gradually after reattachment (s/h ≈ 2.6) in thermal plus chemical non-equilibrium model, a small and gradual rise in the concentration of NO is seen to occur. However, this could possibly be due to the species diffusion, from the peak viscous heating zone, where the formation of NO is relatively high. Such small variations with O_2 and NO are not very apparent in Gupta's [19] model. With respect to N and O, no changes in their mass fractions can be noted. In general, it appears that the species mass fraction do not change in comparison to the freestream values. This would therefore indicate that the shear layer downstream of reattachment is essentially frozen with no gas phase recombination occurring close to the wall and both reaction schemes indicate the same behaviour. It appears, therefore, that the small variation in heat flux is mainly due to the choice of the CFD code. A secondary effect could be through different values of thermal conductivities between the chemical and chemical plus thermal nonequilibrium models that was recently found to influence the difference found in heat flux estimation.The mixing rule for the estimation of transport properties differ in both the real gas models. This would result in small difference in thermal conductivities over the wall. Tchuen and Zeitoun [22], recently compared their finite-rate chemistry simulations with some of the available experiments for high Mach number flows over blunt bodies.They provide detailed comparison of various finite-rate chemistry models and the influence of reaction rates including Park's [9] chemical plus thermal non-equilibrium model. For a wide range of Mach numbers, they show that Park's [9] scheme reasonably models the effects of chemistry in hypersonic flows closely matching experimental data. This lends some confidence in the thermal plus chemical non-equilibrium heat flux data obtained through Park 's [9] model in the present investigation.

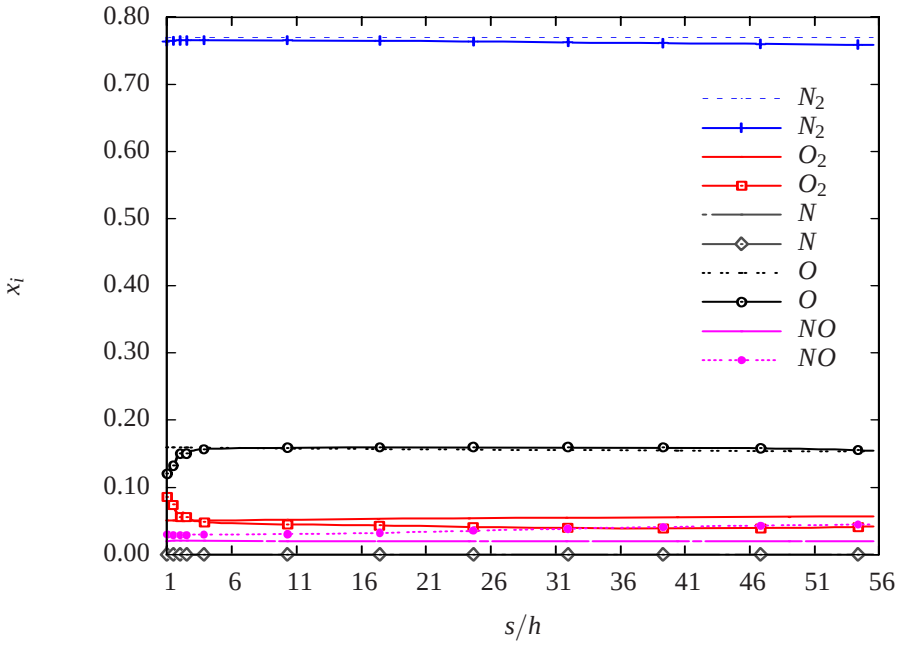

Figure 17. Normalised species mass fraction downstream of the step. Lines with symbol represent thermal plus chemical non-equilibrium (Park's [9]) model and lines without symbols represent chemical non-equilibrium (Gupta's [19]) model

The CFD results obtained by modelling both chemical and thermal non-equilibrium could be visualised from Fig. 18, where the ratio of vibrational-electronic to translational-rotational temperature (T_{v-e}/T_{t-r}) is presented. This ratio indicates the degree of thermal non-equilibrium in the flow. The thermal behaviour in the region upstream of the corner ($s/h \leq 1$) indicates an equilibrium flow in the inviscid region outside the boundary layer, where $T_{v-e}/T_{t-r} \approx 1$. Across the boundary layer, this value decreases indicating a thermal non-equilibrium even though the boundary layer itself is frozen. While the flow expands over the sharp corner, the T_{v-e} increases moderately but generally remains frozen. Within the recirculation region and specifically on the face of the step and up to $s/h \approx 2$ on the plate, $T_{v-e}/T_{t-r} \approx 1$ suggesting the flow there is in thermal equilibrium. This is supported by heat flux data (see Fig. 15(b) and 16) where no differences could be seen between perfect-gas, chemical non-equilibrium and chemical plus thermal non-equilibrium predictions. Even after the shear-layer reattaches, the flow remains in a thermally frozen state.

It should however be noted at this point, that the air-chemistry at high enthalpy conditions involves multiple reactions which have complicated interactions between dissociation-recombination, ionisation and vibrational energy coupling [23]. From a CFD modelling perspective, the greatest uncertainty in air-chemistry can be via reaction rates and thermo-chemical coupling processes [22, 20]. As Sarma [20] notes, this continues to be a basic problem as more reactions are considered in modelling. This also means that uncertainties and difficulties exist in resolving discrepancies that originate solely from modelling the chemistry [23].

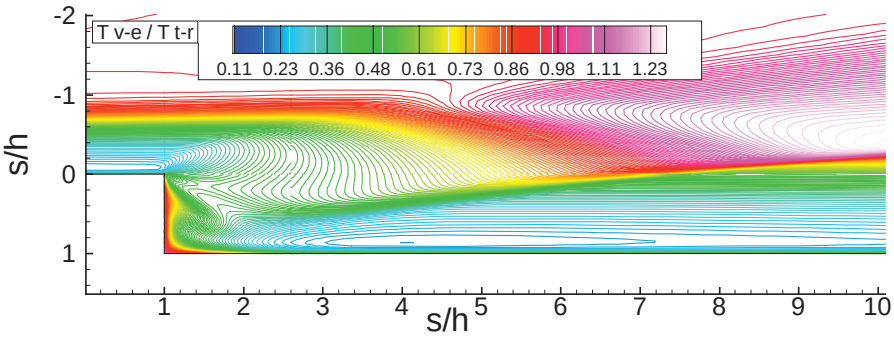

Figure 18. Contour map of the ratio of vibrational-electronic to translational-rotational temperature (T_{v-e}/T_{t-r})

5. CONCLUSIONS

A computational study of heat flux has been carried out for the flow past a rearward facing step in high enthalpy hypersonic flow. To our knowledge, CFD studies at such high enthalpies have not been attempted before. A detailed grid independence analysis has been carried out and the flow separation and reattachment behind the step have been investigated. Effects of real-gas behaviour have been considered through modelling of both chemical and thermal non-equilibrium using some of the well known reaction schemes. The results of CFD simulations have been compared with the experimental data downstream of the step. It is shown that while CFD predictions are reasonable up to about 30 step heights downstream, some significant differences in comparison with experiment are seen in the far downstream region. Effects of chemical and thermal non-equilibrium both show that the flow immediately behind the step is predominantly in the frozen state, except on the step-face and within about a step height on the plate where it is in thermal equilibrium.

ACKNOWLEDGEMENTS

The authors would like to express their sincere thanks to Dr. Peter Jacobs of the University of Queensland for allowing us to use his MB-CNS-2 and Eilmer-3 solvers. Thanks are also due to Daniel

Potter of University of Queensland and Dr. Rowan Gollan of NASA Langley Research Center for their support in explaining various intricacies in these solvers and its usability. We also wish to express our thanks to Professor Richard Hillier of Imperial College, London for allowing us to compare his initial numerical simulations on the present configuration.

REFERENCES

1. S. L. Gai, N. T. Reynolds, C. Ross, and J. P. Baird. Measurements of heat transfer in separated high-enthalpy dissociated laminar hypersonic flow behind a step. *Journal of Fluid Mechanics*, 199:541–561, 1989.
2. M. J. Hayne, S. L. Gai, R. Hillier, R. G. Morgan, D. J. Mee, and T. J. McIntyre. Heat transfer and flow behind a rearward facing step in a super-orbital expansion tube. In *23rd international symposium on shock waves, 22 -27 July 2002, Fort Worth, Texas, USA, In: Lu,F.K., editor, Fort Worth, University of Texas, 2002, Pages: 1574 -1580*, pages 1574–1580, July 2002.
3. M. J. Hayne. *Hypervelocity Flow Over Rearward-Facing Steps*. PhD thesis, Department of Mechanical Engineering, University of Queensland, March 2004.
4. Michael S. Holden. Establishment time of laminar separated flows. *AIAA Journal*, 9(11):2296–2298, 1971.
5. Josef Rom and Arnan Seginer. Laminar heat transfer to a two-dimensional backward facing step from the high-enthalpy supersonic flow in the shock tube. *AIAA Journal*, 2(2):251–255, Feb 1964.
6. S. L. Gai, M. J. Hayne, A. D. Gardner, R. G. Morgan, and D. J. Mee. Heat transfer behind a step in high enthalpy super-orbital flow. In *Proceedings of the 39th Aerospace Sciences Meeting and Exhibit, Reno, Nevada*, Jan 2001.
7. P. A. Jacobs. Mb-cns: a computer program for the simulation of transient compressible flows. Technical Report Report 10/96, Department of Mechanical Engineering, University of Queensland, Brisbane, December 1996.
8. P. A. Jacobs and R. J. Gollan. The eilmer3 code. Technical Report Report 2008/07, Department of Mechanical Engineering, University of Queensland, Brisbane, May 2010.
9. Chul Park. Review of chemical-kinetic problems of future nasa missions, i: Earth entries. *Journal of Thermophysics and Heat Transfer*, 7(3), July-Sept 1993.
10. W. K. Anderson and J. L. Thomas. A comparison of finite volume flux vector splittings for the euler equations. *AIAA*, 24(9):1453–1460, 1986.
11. Y. Wada and M. S. Liou. A flux splitting scheme with high-resolution and robustness for discontinuities. In *Aerospace Sciences Meeting and Exhibit, 32nd, Reno, NV, Jan 10-13, 1994*, number AIAA-1994-83, 1994.
12. P. A. Jacobs. Single-block navier-stokes integrator. Technical Report ICASE Interim Report 18, NASA Langley Research Center, Hampton, VA, July 1991.
13. P. A. Jacobs. Numerical simulation of transient hypervelocity flow in an expansion tube. *Computers & Fluids*, 23(1):77–101, Jan 1994.
14. I. A. Johnston. *Simulation of Flow Around Hypersonic Blunt-Nosed Vehicles for the Calibration of Air Data Systems*. PhD thesis, Department of Mechanical Engineering, University of Queensland, Jan 1999.
15. I. A. Johnston, S. L. Tuttle, P. A. Jacobs, and T. Shimoda. The numerical and experimental simulation of hypervelocity flow around the hyflex vehicle forebody. *Shock Waves*, 9(1):57–67, Feb 1999.
16. V. Wheatley, H. S. Chiu, P. A. Jacobs, M. N. Macrossan, D. J. Mee, and R. G. Morgan. Rarefied, superorbital flows in an expansion tube. *International Journal of Numerical Methods for Heat & Fluid Flow*, 14(4):512– 537, 2004.

17. P. A. Jacobs, T. B. Silvester, R. G. Morgan, M. P. Scott, R. J. Gollan, and T. J. McIntyre. Superorbital expansion tube operation:estimates of flow conditions via numerical simulation. In *43rd AIAA Aerospace Sciences Meeting and Exhibit, 10-13 January 2005, Reno, Nevada*. AIAA, 2005.
18. Mpi: A message-passing interface standard, 2009.
19. Roop N. Gupta, Jerrold M. Yos, Richard A. Thompson, and Kam-Pui Lee. A review of reaction rates and thermodynamic and transport properties for an 11-species air model for chemical and thermal nonequilibrium calculations to 30 000 k. Technical Report 1232, NASA, 1990.
20. G. R. S. Sarma. Physico-chemical modelling in hypersonic flow simulation. *Progress in Aerospace Sciences*, 36(3-4):281–349, April 2000.
21. Druguet. M. C, G. Ben-Dor, and D. Zeitoun. The interaction of supersonic and hypersonic flows with a double cone: comparison between inviscid, viscous, perfect and real gas model simulations. In *26th International Symposium on Shock Waves, Gottingen, Germany*, volume 2, pages 1527–1532, July 2007.
22. Ghislain Tchuen and David E. Zeitoun. Effects of chemistry in nonequilibrium hypersonic flow around blunt bodies. *Journal of Thermophysics and Heat Transfer*, 23(3):433–442, July-Sept 2009.
23. Ioannis Nompelis, Graham V. Candler, Matthew MacLean, Timothy P. Wadhams, and Michael S. Holden. Numerical investigation of double-cone flow experiments with high-enthalpy effects. In *48th AIAA Aerospace Sciences Meeting Including the New Horizons Forum and Aerospace Exposition in Orlando, Florida, 4-7 Jan 2010*, number AIAA 2010-1283. AIAA, Jan 2010.
24. G. Park, S. L. Gai, and A. J. Neely. Aerothermodynamics behind a blunt boday at superorbital speeds. *AIAA Journal*, 48(8):1804–1816, 2010.
25. S. Gordon and B. J. McBride. Computer program for calculation of complex chemical equilibrium compositions and applications: I analysis. Technical Report NASA Reference Publication 1311, NASA, 1994.
26. Rowan J. Gollan. Yet another finite-rate chemistry module for compressible flow codes. Technical Report Division Report, Department of Mechanical Engineering, University of Queensland, Brisbane, July 2003.
27. David Ray Mott. *New Quasi-Steady-State and Partial-Equilibrium Methods for Integrating Chemically Reacting Systems*. PhD thesis, The University of Michigan, 1999.
28. ICEM-CFD. Ansys icem cfd., 2008, ansys inc, southpointe 275 technology drive canonsburg, pa 15317, usa, 2008.
29. A. P. Jackson, R. Hillier, and S. Soltani. Experimental and computational study of laminar cavity flows at hypersonic speeds. *Journal of Fluid Mechanics*, 427:329–358, 2001.
30. P. J. Roache. Quantification of uncertainty in computational fluid dynamics. *Annual Review of Fluid Mechanics*, 29:123–160, 1997.
31. AIAA. Policy statement on numerical accuracy and experimental uncertainty. *AIAA Journal*, 32(1):3 (editorial), 1994.
32. P. J Roache, K. N. Ghia, and F. M. White. Editorial policy statement on the control of numerical accuracy. *ASME Journal of Fluids Engineering*, 108:2, 1986.
33. M. J. Hayne, D. J. Mee, R. G. Morgan, S. L. Gai, and T. J. McIntyre. Heat transfer and flow behind a step in high enthalpy superorbital flow. *The Aeronautical Journal*, (2778):435–442, July 2003.
34. S. Goldstein. On laminar boundary-layer flow near a position of separation. *Quart. J. Mech. Applied Math.*, 1:43–69, 1946.
35. K. Stewartson. On the flow near the trailing edge of a flat plate. *Proc. Roy. Soc. A.*, 306(1486):275–290, Sept 1968.

36. A. F. Messiter. Boundary layer flow near the trailing edge of flat plate. *SIAM J. Appl. Math.*, 18:241–257, 1970.
37. P. G. Daniels. Numerical and asymptotic solutions for the supersonic flow near the trailing edge of a flat plate. *Quart. J. Mech. Applied Math.*, XXVII(2):175–191, 1974.
38. Francis R. Hama. Experimental studies on the lip shock. *AIAA Journal*, 6(2):212–219, Feb 1968.
39. S. Weinbaum. On the singular points in the laminar two-dimensional near wake flow field. *Journal of Fluid Mechanics*, 33(1):39–63, 1968.
40. M. J. Hayne, D. J. Mee, S. L. Gai, and T .J. McIntyre. Boundary layers on a flat plate at sub-and superorbital speeds. *Journal of Thermophysics and Heat Transfer*, 21(4):772–779, Oct-Dec 2007.